



ATLAS CONF Note

ATLAS-CONF-2020-045

3rd August 2020



Observation of vector-boson-fusion production of Higgs bosons in the $H \rightarrow WW^* \rightarrow e\nu\mu\nu$ decay channel in pp collisions at $\sqrt{s} = 13$ TeV with the ATLAS detector

The ATLAS Collaboration

An observation of vector-boson-fusion (VBF) production of Higgs bosons in the $H \rightarrow WW^* \rightarrow e\nu\mu\nu$ decay channel is presented. The proton-proton collision data used to obtain this result were produced at the LHC with a center-of-mass energy of 13 TeV and recorded with the ATLAS detector between 2015 and 2018, corresponding to an integrated luminosity of 139 fb^{-1} . The signal is observed (expected) with a significance of 7.0 (6.2) standard deviations. The product of the total VBF cross-section times the $H \rightarrow WW^*$ branching fraction is measured to be 0.85 ± 0.10 (stat.) $^{+0.17}_{-0.13}$ (syst.) pb, compatible with the Standard Model prediction of 0.81 ± 0.02 pb.

ATLAS-CONF-2020-045
14 August 2020



1 Introduction

This note describes the observation of vector-boson-fusion (VBF) production of Higgs bosons in the $H \rightarrow WW^* \rightarrow e\nu\mu\nu$ decay channel in proton-proton (pp) collisions at a centre-of-mass energy of 13 TeV recorded with the ATLAS detector during the Run 2 data-taking of the Large Hadron Collider (LHC) [1] corresponding to an integrated luminosity of 139 fb^{-1} . This channel has previously been studied by the CMS [2, 3] and ATLAS [4, 5] collaborations using a partial Run 2 dataset corresponding to an integrated luminosity of approximately 36 fb^{-1} and at lower centre-of-mass energies of 8 TeV and 7 TeV during the Run 1 of the LHC. Compared to the previous Run 2 result from ATLAS, several improvements that bring a significant increase in the analysis sensitivity have been incorporated in addition to the increase in data statistics - most notably, refinements in object selection together with an increased number of Monte Carlo (MC) simulated events, as well as a new multi-variate discriminant using a Deep Neural Network (DNN).

2 The ATLAS detector

The ATLAS experiment [6] at the LHC is a multi-purpose particle detector with a forward-backward symmetric cylindrical geometry and a near 4π coverage in solid angle.¹ It consists of an inner tracking detector surrounded by a thin superconducting solenoid providing a 2 T axial magnetic field, electromagnetic and hadron calorimeters, and a muon spectrometer. The inner tracking detector covers the pseudorapidity range $|\eta| < 2.5$. It consists of silicon pixel, silicon microstrip, and transition radiation tracking detectors. An additional pixel layer closest to the beampipe called the insertable b -layer was installed during the long shutdown period prior to the start of Run 2 which provides, among other benefits, an improved resolution of track impact parameters. Lead/liquid-argon (LAr) sampling calorimeters provide electromagnetic (EM) energy measurements with high granularity. A hadron (steel/scintillator-tile) calorimeter covers the central pseudorapidity range ($|\eta| < 1.7$). The end-cap and forward regions are instrumented with LAr calorimeters for both EM and hadronic energy measurements up to $|\eta| = 4.9$. The muon spectrometer surrounds the calorimeters and is based on three large air-core toroidal superconducting magnets with eight coils each. The field integral of the toroids ranges between 2.0 and 6.0 T m across most of the detector. The muon spectrometer includes a system of precision tracking chambers and fast detectors for triggering. A two-level trigger system is used to select events. The first-level trigger is implemented in hardware and uses a subset of the detector information to reduce the accepted rate to at most nearly 100 kHz. This is followed by a software-based trigger that reduces the accepted event rate to 1 kHz on average depending on the data-taking conditions.

3 Signal and background predictions

Higgs boson production and decay into a pair of W bosons are simulated for each of the four main production modes: gluon fusion (ggF), VBF, and associated WH / ZH productions². All signal samples

¹ ATLAS uses a right-handed coordinate system with its origin at the nominal interaction point (IP) in the centre of the detector and the z -axis along the beam pipe. The x -axis points from the IP to the centre of the LHC ring, and the y -axis points upwards. Cylindrical coordinates (r, ϕ) are used in the transverse plane, ϕ being the azimuthal angle around the z -axis. The pseudorapidity is defined in terms of the polar angle θ as $\eta = -\ln \tan(\theta/2)$. Angular distance is measured in units of $\Delta R \equiv \sqrt{(\Delta\eta)^2 + (\Delta\phi)^2}$.

² The $t\bar{t}H$ production mode is not included as its contribution is found to be negligible.

are generated with a Higgs boson mass of 125 GeV.

VBF events are generated with POWHEG [7–10], interfaced with PYTHIA 8.230 [11] with the dipole recoil option on to model the parton shower, hadronisation and underlying event. The POWHEG prediction is accurate to next-to-leading order (NLO) in QCD corrections and tuned to match calculations with effects due to finite heavy-quark masses and soft-gluon resummations up to next-to-next-to-leading-logarithm (NNLL). The MC prediction is normalised to an approximate-NNLO QCD cross section with NLO electroweak corrections [12–14].

The uncertainty due to the parton shower and hadronisation model is evaluated using the same generated events with POWHEG but interfaced to an alternative showering program HERWIG 7 [15, 16]. To estimate the uncertainty related to the matching between the matrix element and the parton shower, MC events produced with the MADGRAPH [17] generator and interfaced to HERWIG 7 are used. They are accurate to NLO in QCD corrections and utilize the NNPDF30_nlo_as_0118 [18] parton distribution function (PDF) set. In both cases, the H7UE set of tuned parameters [16] and the MMHT2014LO PDF set [19] are used for the underlying event.

The ggF production is simulated at NNLO accuracy in QCD using the POWHEG NNLOPS program [7–9, 20, 21], interfaced with PYTHIA 8.212 for parton shower and non-perturbative effects. The simulation achieves NNLO accuracy for arbitrary inclusive $gg \rightarrow H$ observables by reweighting the Higgs boson rapidity³ spectrum in HJ-MiNLO [22–24] to that of HNNLO [25]. The gluon fusion prediction from the MC samples is normalised to the N³LO cross section in QCD plus electroweak corrections at NLO [26–36].

Higgs boson production in association with a vector boson (WH and ZH , collectively referred to as VH) is simulated using POWHEG and interfaced with PYTHIA 8.212 for parton shower and non-perturbative effects. The POWHEG prediction is accurate to NLO for the production of VH boson plus one jet. The MC prediction is normalised to cross sections calculated at NNLO in QCD with NLO electroweak corrections [37–41].

The VBF, ggF, and VH Higgs boson samples use the PDF4LHC15 [42] PDF set and the AZNLO tune [43] of PYTHIA 8.

All Higgs boson sample normalisations account for the decay branching ratios calculated with HDECAY [44–46] and PROPHECY4F [47–49].

For the SM background samples, the QCD-induced WW , WZ , and ZZ processes are simulated with the SHERPA 2.2.2 [50] generator. Fully leptonic final states are generated using matrix elements at NLO accuracy in QCD for up to one additional parton and at LO accuracy for up to three additional parton emissions. Samples for the loop-induced processes $gg \rightarrow VV$ are generated using LO-accurate matrix elements for up to one additional parton emission. Electroweak diboson production in association with two jets ($VVjj$) is generated using SHERPA 2.1.1 [50] with LO-accurate matrix elements.

The production of $V\gamma$ final states is simulated with the SHERPA 2.2.2 [50] generator. Matrix elements are at NLO QCD accuracy for up to one additional parton and at LO accuracy for up to three additional parton emissions.

For all diboson samples, the matrix element calculations are matched and merged with the SHERPA parton shower based on Catani-Seymour dipole factorisation [51, 52] using the MEPS@NLO prescription [53–56]. The virtual QCD correction are provided by the OPENLOOPS library [57, 58]. The NNPDF3.0nnlo set of

³ The rapidity is defined in terms of a particle’s energy E and momentum in the direction of the beam pipe p_z as $y = \frac{1}{2} \ln \frac{E+p_z}{E-p_z}$.

PDFs is used, along with the dedicated set of tuned parton-shower parameters developed by the SHERPA authors.

The QCD-induced production of Z +jets is simulated with the SHERPA 2.2.1 [50] generator using NLO matrix elements for up to two partons, and LO matrix elements for up to four partons calculated with the Comix and OPENLOOPS libraries. They are matched with the SHERPA parton shower [52] using the MEPS@NLO prescription. The NNPDF3.0nnlo set of PDFs is used and the samples are normalised to an NNLO prediction [59]. Electroweak production of $\ell\ell jj$ final states are also generated with SHERPA 2.2.1, but using leading order (LO) matrix elements with up to two additional parton emissions.

The production of $t\bar{t}$ events is modelled using the POWHEGBox v2 generator at NLO with the NNPDF3.0nnlo PDF set and the h_{damp} parameter⁴ set to $1.5 m_{\text{top}}$ [60]. In order to correct for a known mismodeling of the leading lepton p_T due to missing higher-order corrections, an NNLO reweighting is applied to the sample [61]. The events are interfaced to PYTHIA 8.230 to model the parton shower, hadronisation, and underlying event, with parameters set according to the A14 tune and using the NNPDF2.3lo set of PDFs [62]. The decays of bottom and charm hadrons are performed by EVTGEN v1.6.0.

The associated production of top quarks with W bosons (mainly tW) is modelled using the POWHEGBox v2 generator at NLO in QCD using the five-flavour scheme and the NNPDF3.0nnlo set of PDFs. The diagram removal scheme [63] is used to remove interference and overlap with $t\bar{t}$ production. The events are interfaced to PYTHIA 8.230 using the A14 tune and the NNPDF2.3lo set of PDFs. The decays of bottom and charm hadrons are performed by EVTGEN v1.6.0.

The W +jets background is estimated from data, while MC samples are used to validate the estimate and to determine the flavour composition uncertainties. These MC samples are generated using POWHEG interfaced with PYTHIA 8.

For all MC samples, the effect of additional pp interactions in the same and neighbouring bunch crossings (pile-up) is modelled by overlaying simulated inelastic pp events generated with PYTHIA 8.186 [64] using the NNPDF2.3lo set of PDFs and the A3 tune [65] over the original hard-scattering event.

4 Event selection and multivariate analysis

Events are triggered using a combination of single-lepton triggers and a dilepton $e\mu$ trigger in order to maximize the total trigger efficiency. The transverse momentum threshold for single-electron(muon) triggers is 24(20) GeV for the first year of data taking, while it is increased to 26 GeV for both lepton flavours during the remainder of Run 2. The $e\mu$ trigger requires a minimum p_T threshold of 17 GeV for electrons [66] and 14 GeV for muons [67].

Electron candidates are reconstructed through association of energy clusters in the electromagnetic calorimeter with well-reconstructed tracks that are extrapolated to the calorimeter [68]. Electrons are required to satisfy $|\eta| < 2.47$, excluding the transition region $1.37 < |\eta| < 1.52$ between the barrel and end-caps in the LAr calorimeter. Muon candidates are reconstructed from a global fit of matched tracks from the inner detector and the muon spectrometer [69]. They are required to satisfy $|\eta| < 2.5$. In order to reject particles misidentified as prompt leptons, several identification requirements as well as isolation and impact parameter criteria [69, 70] are applied. For electrons, a likelihood-based identification method [70]

⁴ The h_{damp} parameter is a resummation damping factor and one of the parameters that controls the matching of POWHEG matrix elements to the parton shower and thus effectively regulates the high- p_T radiation against which the $t\bar{t}$ system recoils.

is employed, which takes into account a number of discriminating variables such as shower shapes, track properties, and track-cluster-matching. For muons, a quality-based identification method [69] is employed, selected a working point with a relatively lower efficiency (although still $\sim 95\%$) so as to maximize the sample purity. The impact parameter requirements are $|z_0 \sin \theta| < 0.5$ mm and $|d_0|/\sigma_{d_0} < 5$ (3) for electrons (muons)⁵. Maximum thresholds in terms of both energy (using close-by clusters in the calorimeter) and p_T (using close-by tracks) are taken into account when defining the lepton isolation working points. At least one of the offline reconstructed leptons must be matched to an online object that triggered the recording of the event. In the case where the $e\text{--}\mu$ trigger is solely responsible for the recording of the event, each lepton must correspond to one of the trigger objects. This trigger matching scheme also requires the p_T of the lepton to be at least 1 GeV above the trigger level threshold. Jets are reconstructed using the anti- k_t algorithm with a radius parameter of $R = 0.4$ and particle flow objects as input [71, 72]. The energy of the jets is corrected for the non-compensating calorimeter response, noise threshold effects, energy loss from inactive material, and pile-up contamination [73]. For jets entering the analysis, a kinematic selection of $p_T > 20$ GeV and $|\eta| < 4.5$ is applied. Furthermore, a multivariate selection that reduces contamination from pile-up [74] is applied to jets with $20 < p_T < 60$ GeV and $|\eta| < 2.4$, utilizing calorimeter and tracking information to separate hard-scatter jets from pile-up jets. Jets with $p_T > 20$ GeV and $|\eta| < 2.5$ containing b -hadrons (b -jets) are identified using a neural network discriminant based on a number of lower level taggers which utilize relevant quantities such as the associated track impact parameters and information from secondary vertices. A working point with an average 85% b -jet tagging efficiency is adopted, as estimated from simulated $t\bar{t}$ events [75, 76]. The missing transverse momentum E_T^{miss} (with magnitude E_T^{miss}) is defined as the negative vector sum of the p_T of all the selected leptons and jets, together with reconstructed tracks that are not associated with these objects but are consistent with originating from the primary pp collision [77].

The full event selection is summarized in Table 1. Events are first selected by requiring exactly two⁶ different-flavour opposite-sign leptons, the higher- p_T (leading) lepton with $p_T > 22$ GeV and the subleading lepton with $p_T > 15$ GeV. In addition, there must be at least two jets in the event with $p_T > 30$ GeV where the two leading jets are tagged as originating from the VBF process. To reject background from top-quark production, events containing b -jets with $p_T > 20$ GeV are vetoed. The invariant mass of the hypothetical τ -lepton pair ($m_{\tau\tau}$), calculated using the collinear approximation [78], is also used to veto background from $Z \rightarrow \tau\tau$ production. In order to further enhance the VBF topology, events are rejected if they contain either additional jets with $p_T > 30$ GeV that lie in the interval between the two tagging jets in pseudo-rapidity (a central jet veto) or either lepton outside the interval between the two tagging jets in pseudo-rapidity (an outside lepton veto). The signal region (SR) is defined by applying all of the above selection criteria.

In order to fully exploit the distinct event topology of the VBF signal, a multivariate analysis based on a DNN is implemented through keras [79] and TensorFlow [80]. Kinematic variables built from the leptons (ℓ), jets (j), and E_T^{miss} in the event are used as inputs to the DNN training. The following variables are chosen to provide discrimination based on the VBF topology: the invariant mass of the two leading jets (m_{jj}), the difference between the two jet rapidities (Δy_{jj}), the lepton η -centrality ($\sum_{\ell} C_{\ell}$, where $C_{\ell} = |2\eta_{\ell} - \sum \eta_j|/\Delta\eta_{jj}$), which quantifies the positions of the leptons relative to the leading jets in pseudorapidity [81], the p_T of the three leading jets ($p_T^{\text{jet}_1}, p_T^{\text{jet}_2}, p_T^{\text{jet}_3}$, where $p_T^{\text{jet}_3}$ is set to 0 GeV if there is no third jet in the event), and the invariant masses of all four possible lepton–jet pairs between the leptons

⁵ z_0 and d_0 are the longitudinal and transverse impact parameters, respectively, defined in terms of the point of closest approach between the associated track and the hard-scatter primary vertex.

⁶ The isolation criteria for additional leptons that are vetoed is looser than the nominal working point used for the two leading leptons and in the case of additional muons, a medium identification quality [69] is used.

	Signal region	Z+jets CR	Top quark CR
Pre-selection	Two isolated, different-flavour leptons ($\ell = e, \mu$) with opposite charge $p_T^{\text{lead}} > 22 \text{ GeV}$, $p_T^{\text{sublead}} > 15 \text{ GeV}$ $m_{\ell\ell} > 10 \text{ GeV}$, $N_{\text{jet}} \geq 2$ $N_{b\text{-jet}, (p_T > 20 \text{ GeV})} = 0$		
Selection	$m_{\tau\tau} < m_Z - 25 \text{ GeV}$ $m_{jj} > 120 \text{ GeV}$ –	$ m_{\tau\tau} - m_Z < 25 \text{ GeV}$ – $m_{\ell\ell} < 70 \text{ GeV}$ central jet veto outside lepton veto	$m_{\tau\tau} < m_Z - 25 \text{ GeV}$ – –
A DNN is applied in the SR that uses 15 discriminant variables: $\Delta\phi_{\ell\ell}, m_{\ell\ell}, m_T, \Delta y_{jj}, m_{jj}, p_T^{\text{tot}}, \sum_{\ell} C_{\ell}, m_{\ell_1 j_1}, m_{\ell_1 j_2}, m_{\ell_2 j_1}, m_{\ell_2 j_2},$ $p_T^{\text{jet}_1}, p_T^{\text{jet}_2}, p_T^{\text{jet}_3}$, and E_T^{miss} significance			

Table 1: Event selection criteria used to define the signal and control regions in the analysis. Definitions including the p_T thresholds for jet counting are given in the text. For leptons that are matched to the trigger, the lepton p_T requirements are applied in addition to the trigger matching scheme, which requires the p_T of the lepton to be at least 1 GeV above the trigger level threshold.

and the two leading jets ($m_{\ell_1 j_1}, m_{\ell_1 j_2}, m_{\ell_2 j_1}, m_{\ell_2 j_2}$). Three variables targeting the $H \rightarrow WW^*$ decay topology are also utilized: the invariant mass of the two leptons ($m_{\ell\ell}$), the difference between the azimuthal angles of the two leptons ($\Delta\phi_{\ell\ell}$), and the dilepton+ E_T^{miss} transverse mass (m_T). Finally, two additional variables are included in order to suppress events containing top quarks, the leading background in the analysis: the total transverse momentum (p_T^{tot}) is defined as the magnitude of the vectorial sum of the p_T of all selected objects, while the E_T^{miss} significance provides separation between events with real undetected high- p_T particles and events where the E_T^{miss} is the result of resolution effects [82]. The DNN output reflects the compatibility of an event with having VBF-like kinematics and thus is used as a classifier, with the signal purity improving as the output value increases. The DNN output is used as the discriminating variable in the statistical analysis, with seven bins in total. The bin boundaries are chosen with an algorithm that aims to split the bins as finely as possible, while also requiring at least 10 expected signal and background events each per bin as well as a maximum relative statistical uncertainty on the background of 20%, yielding smaller bin widths on average for larger values of the DNN output. When these criteria are satisfied, a bin boundary is set once there are more than 20 signal events present in a given bin. In the bin with the highest DNN output, the expected VBF signal-to-background ratio is approximately 3.5. The DNN output distribution in the final signal region is presented in Figure 1.

5 Background estimation

Several processes contribute to the background contamination in the SR: non-resonant WW , top-quark pair ($t\bar{t}$) and single-top-quark (Wt), other diboson ($WZ, ZZ, W\gamma, W\gamma^*$) and Drell-Yan (mainly $Z \rightarrow \tau\tau$, hereafter denoted Z+jets) production. Background processes with mis-identified leptons are commonly denoted as Mis-Id, which are primarily composed of W+jets but also include the contribution from multi-jet events with more than one mis-identified lepton as well as a minor contribution of semi-leptonic $t\bar{t}$. Higgs

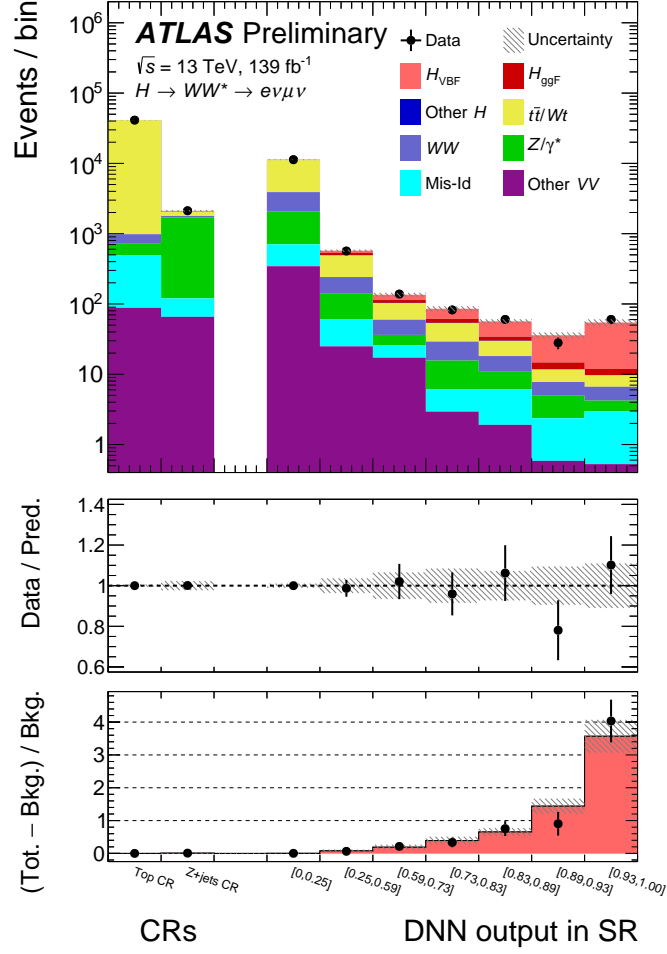


Figure 1: Post-fit distribution of the DNN output in the VBF signal region, together with the top quark and Z+jets control regions. The hatched band shows the total uncertainty of the signal and background modelled contributions. The middle panel shows the ratio of the data to the sum of the fitted signal and background. The bottom panel displays the signal to background ratio, where the hatched band indicates the combined statistical and systematic uncertainty for the fitted signal and background.

boson production through mechanisms other than VBF are fixed to their SM expectations and treated as backgrounds in the analysis.

The observed yields in dedicated control regions (CRs) are used to normalise the expected top-quark⁷ and Z+jets backgrounds in the SR. The CR selections are also summarized in Table 1. The top quark CR is made orthogonal to the SR by requiring exactly one b -tagged jet instead of vetoing events with b -tagged jets and is 98% pure in top quark backgrounds. The post-fit normalisation factor for the top-quark backgrounds is found to be $1.02^{+0.17}_{-0.13}$. The post-fit Δy_{jj} distribution for events in the top quark CR is presented in Fig. 2(a). The Z+jets CR is made orthogonal to the SR by inverting the $Z \rightarrow \tau\tau$ veto: $|m_{\tau\tau} - m_Z| < 25$ GeV. It is 78% pure in Z+jets events. The post-fit normalisation factor for Z+jets is found to be $0.94^{+0.25}_{-0.20}$. The post-fit Δy_{jj} distribution for events in the Z+jets CR is presented in Fig. 2(b).

⁷ The $t\bar{t}$ and Wt processes are normalized together using a single factor.

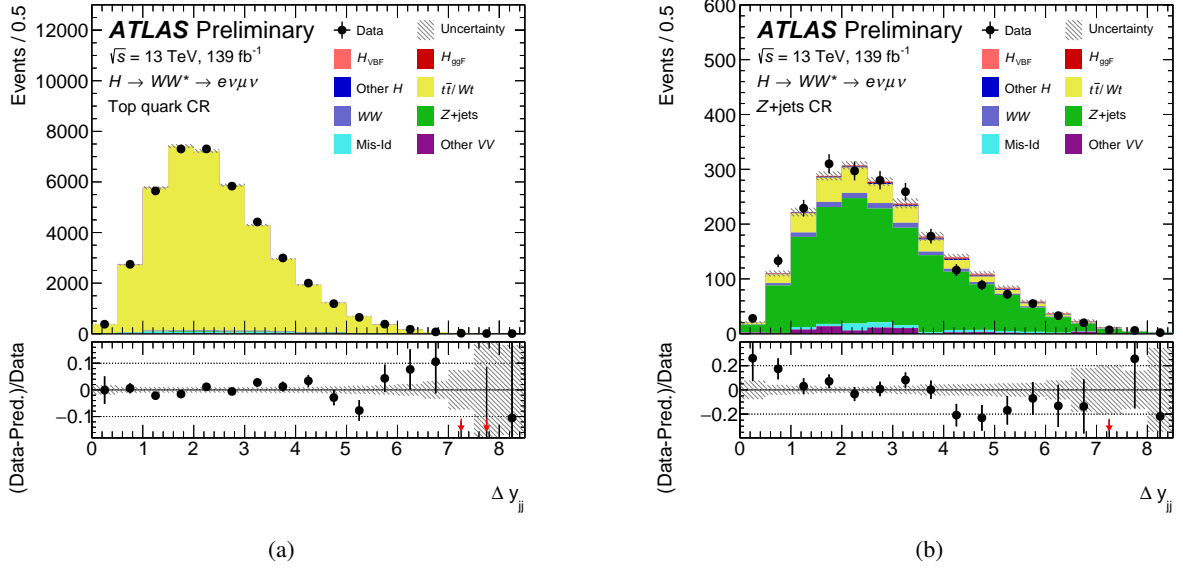


Figure 2: Post-fit Δy_{jj} distribution in the (a) top quark and (b) Z+jets control regions. The red arrows in the sub-panel denote where the central value of the data lies above or below the window. Each of the processes are normalized to their post-fit yields in the corresponding CR. The hatched band shows the post-fit uncertainties derived from propagating the relative normalization uncertainty for each process to the post-fit distribution. Uncertainties due to shape variations are not accounted for in the uncertainty bands.

The Mis-Id background is estimated using a data-driven technique where control samples are used in which all nominal selections are applied with the exception that one of the two lepton candidates fails to meet the full identification criteria, but satisfies a looser set of identification criteria (referred to as an anti-identified lepton). The expected yields from the Mis-Id background in the SR, top quark CR, and Z+jets CR are extrapolated from the observed number of events in the corresponding control samples, after subtracting the expected contribution from processes with two prompt leptons [5]. The small contribution from processes with two misidentified leptons are accounted for in the extrapolation by applying a correction term evaluated in a sample where both lepton candidates are anti-identified. The correction makes up about 25% of the total misidentified lepton yield. The extrapolation factor is determined in a sample of Z+jets-enriched events, where the Z boson decays to a same-flavour pair of electrons or muons, and the misidentified lepton candidate recoils against the Z boson. It is defined as the ratio of the numbers of events in which the misidentified lepton candidate is identified and anti-identified, and is measured in bins of lepton p_T and $|\eta|$. A correction factor is used to account for the fact that the Z+jets-enriched sample in which the extrapolation factor is derived and the largest background source in the signal region (W+jets) exhibit different compositions of sources of misidentified leptons, such as hadrons, non-prompt leptons from heavy-flavour decays and photons. The sample composition correction factor is determined from the ratio of extrapolation factors measured in W+jets and Z+jets MC simulation.

6 Systematic uncertainties

Uncertainties from both experimental and theoretical origins are assigned to the results. The dominant experimental uncertainties are due to the E_T^{miss} measurement [77]. Other sources of experimental uncertainty

include jet energy scale and resolution [73], lepton energy (momentum) scale and resolution, identification and isolation [69, 70], b -tagging efficiency [76], trigger uncertainties [66, 67], modelling of pile-up, and luminosity measurement [83]. The luminosity uncertainty is only applied to the Higgs boson signal and to background processes that are normalised to theoretical predictions. All the aforementioned experimental uncertainties have been considered also for their impact on the DNN shape, except in the case where no evidence for a significant systematic variation is observed. Three sources of uncertainty related to the extrapolation factor used in the data-driven Mis-Id background estimate are considered: the statistical uncertainty on the extrapolation factor itself, an uncertainty related to the subtraction of processes with two prompt leptons from the Z +jets-enriched sample used to derive the extrapolation factor, and an uncertainty in the sample composition correction factor. While the relative size of these three uncertainties depends on the specific bin of the extrapolation factor, they collectively have only a minimal impact on the overall signal strength.

Theoretical uncertainties are assessed through QCD renormalisation and factorisation scale variations. For the main processes, the impact from different matrix element and non-perturbative effects are estimated by a comparison between nominal and alternative generators. For the prediction of $qqWW$ and of WZ , ZZ , $V\gamma^*$, and $V\gamma$ production (VV), variations of the matching scale and non-perturbative effects are considered instead of an alternative program. In addition, the effects of PDF model uncertainties are evaluated. The dominant source of uncertainty on the signal strength originates from the VBF parton shower uncertainty, which is taken as a comparison between the nominal MC sample and the prediction with an alternative parton shower. The second largest theoretical uncertainty is due to the matching in the VBF signal samples and is derived from a comparison between the POWHEG + HERWIG 7 and MADGRAPH + HERWIG 7 signal MC samples. In both cases, the primary components originate from shape differences in the DNN output.

7 Signal region yields and results

The signal strength parameter μ_{VBF} is obtained from a simultaneous profile likelihood fit to data in the signal and control regions defined in the previous sections. It is defined as the ratio of the measured signal yield in these regions to that predicted by the Standard Model. The CRs are used to determine the normalisation of the corresponding backgrounds and enter the fit as single bins. The systematic uncertainties enter the fit as nuisance parameters in the likelihood function.

Table 2 shows the post-fit yields for the VBF SR. Yields are shown separately for the highest DNN output bin, which provides the majority of the signal sensitivity. The number of observed signal events is in agreement with the Standard Model expectation. The observed (expected) VBF signal has a significance of 7.0 (6.2) σ above the background expectation. The signal strength for the VBF production mode in the $H \rightarrow WW^*$ decay channel is measured to be

$$\begin{aligned}\mu_{\text{VBF}} &= 1.04^{+0.24}_{-0.20} \\ &= 1.04^{+0.13}_{-0.12} \text{ (stat.) }^{+0.09}_{-0.08} \text{ (exp syst.) }^{+0.17}_{-0.12} \text{ (sig. theo.) }^{+0.08}_{-0.07} \text{ (bkg. theo.)}.\end{aligned}$$

Furthermore, a consistent value is obtained when allowing the ggF background normalization to float freely in the likelihood fit, with the observed significance reduced slightly to 6.3 σ .

The cross-section times branching fraction, $\sigma_{\text{VBF}} \cdot \mathcal{B}_{H \rightarrow WW^*}$, is measured to be

$$\begin{aligned}\sigma_{\text{VBF}} \cdot \mathcal{B}_{H \rightarrow WW^*} &= 0.85^{+0.20}_{-0.17} \text{ pb} \\ &= 0.85 \pm 0.10 \text{ (stat.) }^{+0.08}_{-0.07} \text{ (exp syst.) }^{+0.13}_{-0.10} \text{ (sig. theo.) }^{+0.07}_{-0.06} \text{ (bkg. theo.) pb},\end{aligned}$$

Process	Total	Highest DNN bin
H_{VBF}	209 ± 37	42.5 ± 6.5
H_{ggF}	169 ± 62	2.2 ± 1.5
Other Higgs	28 ± 2.0	0.1 ± 0.3
$t\bar{t}/Wt$	7520 ± 830	3.0 ± 1.7
Z/γ^*	1460 ± 370	1.2 ± 1.1
WW	2000 ± 350	2.4 ± 1.6
Mis-Id	416 ± 58	2.5 ± 1.6
Other VV	392 ± 64	0.5 ± 0.7
Total	12200 ± 120	54.5 ± 6.0
Observed	12189	60

Table 2: Post-fit MC and data yields in the VBF SRs. Yields in the highest DNN output bin are also presented. The quoted uncertainties correspond to the statistical uncertainties, together with the experimental and theory modeling systematics. The sum of all the contributions may differ from the total value due to rounding. Moreover, the total uncertainty differs from the sum in quadrature of the single-process uncertainties due to anti-correlation effects in their systematic sources which dominate over their MC statistical uncertainties.

in comparison to the SM predicted value of 0.81 ± 0.02 pb [26].

Table 3 shows the relative impact of the main uncertainties on the measured value of μ_{VBF} . The measurements of the cross-section times branching fraction and the signal strength are dominated by theory uncertainties, of which VBF signal uncertainties make up the largest contribution.

Source	$\Delta\mu_{\text{VBF}}/\mu_{\text{VBF}} [\%]$
Data statistics	12.5
Total systematics	17.8
Experimental uncertainties	8.8
Missing ET	4.7
MC statistics	3.1
Jet energy scale	2.2
Luminosity	1.9
Modelling of pile-up	1.7
b -tagging	1.6
Jet energy resolution	1.4
Misidentified leptons	0.9
VBF signal theory uncertainties	14.4
Background theory uncertainties	7.7
ggF Higgs	5.2
Top-quark	3.3
WW	2.5
Z+jets	1.9
Total	22

Table 3: Breakdown of impacts on the signal strength μ_{VBF} . The uncertainties are estimated by the breakdown method, in which nuisance parameters associated with the uncertainty group in question are first fixed to their best fit value and the uncertainty on the measured signal strength is recomputed. The quadrature difference between the original and recomputed uncertainties present the impact of the uncertainty group. The uncertainties of the main components were calculated by iteratively fixing the respective sets of nuisance parameters and calculating the quadrature difference to the previous step, in reverse order of display.

8 Conclusions

A search for VBF production of Higgs bosons in the $H \rightarrow WW^*$ decay channel is performed. This result is based on a dataset of proton-proton collisions recorded with the ATLAS detector at the LHC in 2015-2018 at a center-of-mass energy of 13 TeV and corresponds to an integrated luminosity of 139 fb^{-1} . The observed (expected) signal significance is found to be 7.0σ (6.2σ). The product of the total VBF cross-section times the $H \rightarrow WW^*$ branching fraction is measured at 0.85 ± 0.10 (stat.) $^{+0.17}_{-0.13}$ (syst.) pb, compatible with the Standard Model prediction of 0.81 ± 0.02 pb. These results provide an observation of the VBF production of Higgs bosons subsequently decaying to a pair of W bosons.

References

- [1] L. Evans and P. Bryant, *LHC Machine*, [JINST **3** \(2008\) S08001](#) (cit. on p. 2).
- [2] CMS Collaboration, *Measurements of properties of the Higgs boson decaying to a W boson pair in pp collisions at $\sqrt{s} = 13 \text{ TeV}$* , [Phys. Lett. B **791** \(2019\) 96](#), arXiv: [1806.05246 \[hep-ex\]](#) (cit. on p. 2).
- [3] CMS Collaboration, *Observation of a new boson with mass near 125 GeV in pp collisions at $\sqrt{s} = 7$ and 8 TeV*, [JHEP **06** \(2013\) 081](#), arXiv: [1303.4571 \[hep-ex\]](#) (cit. on p. 2).

- [4] ATLAS Collaboration, *Measurements of gluon-gluon fusion and vector-boson fusion Higgs boson production cross-sections in the $H \rightarrow WW^* \rightarrow e\nu\mu\nu$ decay channel in pp collisions at $\sqrt{s} = 13$ TeV with the ATLAS detector*, *Phys. Lett. B* **789** (2019) 508, arXiv: [1808.09054 \[hep-ex\]](#) (cit. on p. 2).
- [5] ATLAS Collaboration, *Observation and measurement of Higgs boson decays to WW^* with the ATLAS detector*, *Phys. Rev. D* **92** (2015) 012006, arXiv: [1412.2641 \[hep-ex\]](#) (cit. on pp. 2, 8).
- [6] ATLAS Collaboration, *The ATLAS Experiment at the CERN Large Hadron Collider*, *JINST* **3** (2008) S08003 (cit. on p. 2).
- [7] P. Nason, *A New method for combining NLO QCD with shower Monte Carlo algorithms*, *JHEP* **11** (2004) 040, arXiv: [hep-ph/0409146](#) (cit. on p. 3).
- [8] S. Frixione, P. Nason and C. Oleari, *Matching NLO QCD computations with Parton Shower simulations: the POWHEG method*, *JHEP* **11** (2007) 070, arXiv: [0709.2092 \[hep-ph\]](#) (cit. on p. 3).
- [9] S. Alioli, P. Nason, C. Oleari and E. Re, *A general framework for implementing NLO calculations in shower Monte Carlo programs: the POWHEG BOX*, *JHEP* **06** (2010) 043, arXiv: [1002.2581 \[hep-ph\]](#) (cit. on p. 3).
- [10] P. Nason and C. Oleari, *NLO Higgs boson production via vector-boson fusion matched with shower in POWHEG*, *JHEP* **02** (2010) 037, arXiv: [0911.5299 \[hep-ph\]](#) (cit. on p. 3).
- [11] T. Sjöstrand et al., *An introduction to PYTHIA 8.2*, *Comput. Phys. Commun.* **191** (2015) 159, arXiv: [1410.3012 \[hep-ph\]](#) (cit. on p. 3).
- [12] M. Ciccolini, A. Denner and S. Dittmaier, *Strong and electroweak corrections to the production of Higgs + 2-jets via weak interactions at the LHC*, *Phys. Rev. Lett.* **99** (2007), arXiv: [0707.0381 \[hep-ph\]](#) (cit. on p. 3).
- [13] M. Ciccolini, A. Denner and S. Dittmaier, *Electroweak and QCD corrections to Higgs production via vector-boson fusion at the LHC*, *Phys. Rev. D* **77** (2008) 013002, arXiv: [0710.4749 \[hep-ph\]](#) (cit. on p. 3).
- [14] P. Bolzoni et al., *Higgs production via vector-boson fusion at NNLO in QCD*, *Phys. Rev. Lett.* **105** (2010), arXiv: [1003.4451 \[hep-ph\]](#) (cit. on p. 3).
- [15] M. Bahr et al., *Herwig++ physics and manual*, *Eur. Phys. J. C* **58** (2008) 639, arXiv: [0803.0883 \[hep-ph\]](#) (cit. on p. 3).
- [16] J. Bellm et al., *Herwig 7.0/Herwig++ 3.0 release note*, *Eur. Phys. J. C* **76** (2016) 196, arXiv: [1512.01178 \[hep-ph\]](#) (cit. on p. 3).
- [17] J. Alwall et al., *The automated computation of tree-level and next-to-leading order differential cross sections, and their matching to parton shower simulations*, *JHEP* **07** (2014) 079, arXiv: [1405.0301 \[hep-ph\]](#) (cit. on p. 3).
- [18] R. D. Ball et al., *Parton distributions for the LHC run II*, *Journal of High Energy Physics* **2015** (2015), ISSN: 1029-8479, URL: [http://dx.doi.org/10.1007/JHEP04\(2015\)040](http://dx.doi.org/10.1007/JHEP04(2015)040) (cit. on p. 3).
- [19] Harland-Lang, L. A., Martin, A. D., Motylinski, P. and Thorne, R. S., *Parton distributions in the LHC era: MMHT 2014 PDFs*, *Eur. Phys. J. C* **75** (2015) 204, URL: <https://doi.org/10.1140/epjc/s10052-015-3397-6> (cit. on p. 3).
- [20] K. Hamilton, P. Nason, E. Re and G. Zanderighi, *NNLOPS simulation of Higgs boson production*, *JHEP* **10** (2013) 222, arXiv: [1309.0017 \[hep-ph\]](#) (cit. on p. 3).

- [21] K. Hamilton, P. Nason and G. Zanderighi, *Finite quark-mass effects in the NNLOPS POWHEG+MiNLO Higgs generator*, *JHEP* **05** (2015) 140, arXiv: [1501.04637 \[hep-ph\]](#) (cit. on p. 3).
- [22] K. Hamilton, P. Nason and G. Zanderighi, *MINLO: Multi-Scale Improved NLO*, *JHEP* **10** (2012) 155, arXiv: [1206.3572 \[hep-ph\]](#) (cit. on p. 3).
- [23] J. M. Campbell et al., *NLO Higgs Boson Production Plus One and Two Jets Using the POWHEG BOX, MadGraph4 and MCFM*, *JHEP* **07** (2012) 092, arXiv: [1202.5475 \[hep-ph\]](#) (cit. on p. 3).
- [24] K. Hamilton, P. Nason, C. Oleari and G. Zanderighi, *Merging $H/W/Z + 0$ and 1 jet at NLO with no merging scale: a path to parton shower + NNLO matching*, *JHEP* **05** (2013) 082, arXiv: [1212.4504 \[hep-ph\]](#) (cit. on p. 3).
- [25] S. Catani and M. Grazzini, *An NNLO subtraction formalism in hadron collisions and its application to Higgs boson production at the LHC*, *Phys. Rev. Lett.* **98** (2007) 222002, arXiv: [hep-ph/0703012](#) (cit. on p. 3).
- [26] D. de Florian et al., *Handbook of LHC Higgs Cross Sections: 4. Deciphering the Nature of the Higgs Sector*, **2/2017** (2016), arXiv: [1610.07922 \[hep-ph\]](#) (cit. on pp. 3, 10).
- [27] C. Anastasiou et al., *High precision determination of the gluon fusion Higgs boson cross-section at the LHC*, *JHEP* **05** (2016) 058, arXiv: [1602.00695 \[hep-ph\]](#) (cit. on p. 3).
- [28] C. Anastasiou, C. Duhr, F. Dulat, F. Herzog and B. Mistlberger, *Higgs Boson Gluon-Fusion Production in QCD at Three Loops*, *Phys. Rev. Lett.* **114** (2015) 212001, arXiv: [1503.06056 \[hep-ph\]](#) (cit. on p. 3).
- [29] F. Dulat, A. Lazopoulos and B. Mistlberger, *iHixs 2 — Inclusive Higgs cross sections*, *Comput. Phys. Commun.* **233** (2018) 243, arXiv: [1802.00827 \[hep-ph\]](#) (cit. on p. 3).
- [30] R. V. Harlander and K. J. Ozeren, *Finite top mass effects for hadronic Higgs production at next-to-next-to-leading order*, *JHEP* **11** (2009) 088, arXiv: [0909.3420 \[hep-ph\]](#) (cit. on p. 3).
- [31] R. V. Harlander and K. J. Ozeren, *Top mass effects in Higgs production at next-to-next-to-leading order QCD: Virtual corrections*, *Phys. Lett. B* **679** (2009) 467, arXiv: [0907.2997 \[hep-ph\]](#) (cit. on p. 3).
- [32] R. V. Harlander, H. Mantler, S. Marzani and K. J. Ozeren, *Higgs production in gluon fusion at next-to-next-to-leading order QCD for finite top mass*, *Eur. Phys. J. C* **66** (2010) 359, arXiv: [0912.2104 \[hep-ph\]](#) (cit. on p. 3).
- [33] A. Pak, M. Rogal and M. Steinhauser, *Finite top quark mass effects in NNLO Higgs boson production at LHC*, *JHEP* **02** (2010) 025, arXiv: [0911.4662 \[hep-ph\]](#) (cit. on p. 3).
- [34] S. Actis, G. Passarino, C. Sturm and S. Uccirati, *NLO Electroweak Corrections to Higgs Boson Production at Hadron Colliders*, *Phys. Lett. B* **670** (2008) 12, arXiv: [0809.1301 \[hep-ph\]](#) (cit. on p. 3).
- [35] S. Actis, G. Passarino, C. Sturm and S. Uccirati, *NNLO Computational Techniques: The Cases $H \rightarrow \gamma\gamma$ and $H \rightarrow gg$* , *Nucl. Phys. B* **811** (2009) 182, arXiv: [0809.3667 \[hep-ph\]](#) (cit. on p. 3).
- [36] M. Bonetti, K. Melnikov and L. Tancredi, *Higher order corrections to mixed QCD-EW contributions to Higgs boson production in gluon fusion*, *Phys. Rev. D* **97** (2018) 056017, [Erratum: *Phys. Rev. D* 97, 099906 (2018)], arXiv: [1801.10403 \[hep-ph\]](#) (cit. on p. 3).
- [37] M. Ciccolini, S. Dittmaier and M. Kramer, *Electroweak radiative corrections to associated WH and ZH production at hadron colliders*, *Phys. Rev. D* **68** (2003) 073003, arXiv: [hep-ph/0306234](#) (cit. on p. 3).

- [38] O. Brein, A. Djouadi and R. Harlander, *NNLO QCD corrections to the Higgs-strahlung processes at hadron colliders*, *Phys. Lett. B* **579** (2004) 149, arXiv: [hep-ph/0307206](#) (cit. on p. 3).
- [39] O. Brein, R. Harlander, M. Wiesemann and T. Zirke, *Top-Quark Mediated Effects in Hadronic Higgs-Strahlung*, *Eur. Phys. J. C* **72** (2012) 1868, arXiv: [1111.0761 \[hep-ph\]](#) (cit. on p. 3).
- [40] A. Denner, S. Dittmaier, S. Kallweit and A. Mück, *HAWK 2.0: A Monte Carlo program for Higgs production in vector-boson fusion and Higgs strahlung at hadron colliders*, *Comput. Phys. Commun.* **195** (2015) 161, arXiv: [1412.5390 \[hep-ph\]](#) (cit. on p. 3).
- [41] O. Brein, R. V. Harlander and T. J. Zirke, *vh@nnlo - Higgs Strahlung at hadron colliders*, *Comput. Phys. Commun.* **184** (2013) 998, arXiv: [1210.5347 \[hep-ph\]](#) (cit. on p. 3).
- [42] J. Butterworth et al., *PDF4LHC recommendations for LHC Run II*, *J. Phys. G* **43** (2016), arXiv: [1510.03865 \[hep-ph\]](#) (cit. on p. 3).
- [43] ATLAS Collaboration, *Measurement of the Z/γ^* boson transverse momentum distribution in pp collisions at $\sqrt{s} = 7$ TeV with the ATLAS detector*, *JHEP* **09** (2014) 145, arXiv: [1406.3660 \[hep-ex\]](#) (cit. on p. 3).
- [44] A. Djouadi, J. Kalinowski and M. Spira, *HDECAY: A Program for Higgs boson decays in the standard model and its supersymmetric extension*, *Comput. Phys. Commun.* **108** (1998) 56, arXiv: [hep-ph/9704448](#) (cit. on p. 3).
- [45] M. Spira, *QCD effects in Higgs physics*, *Fortsch. Phys.* **46** (1998) 203, arXiv: [hep-ph/9705337](#) (cit. on p. 3).
- [46] A. Djouadi, M. Muhlleitner and M. Spira, *Decays of supersymmetric particles: The Program SUSY-HIT (SUSpect-SdecaY-Hdecay-InTerface)*, *Acta Phys. Polon. B* **38** (2007) 635, ed. by K. Fialkowski and B. Muryn, arXiv: [hep-ph/0609292](#) (cit. on p. 3).
- [47] A. Bredenstein, A. Denner, S. Dittmaier and M. Weber, *Radiative corrections to the semileptonic and hadronic Higgs-boson decays $H \rightarrow WW/ZZ \rightarrow 4$ fermions*, *JHEP* **02** (2007) 080, arXiv: [hep-ph/0611234](#) (cit. on p. 3).
- [48] A. Bredenstein, A. Denner, S. Dittmaier and M. Weber, *Precise predictions for the Higgs-boson decay $H \rightarrow WW/ZZ \rightarrow 4$ leptons*, *Phys. Rev. D* **74** (2006) 013004, arXiv: [hep-ph/0604011](#) (cit. on p. 3).
- [49] A. Bredenstein, A. Denner, S. Dittmaier and M. Weber, *Precision calculations for the Higgs decays $H \rightarrow ZZ/WW \rightarrow 4$ leptons*, *Nucl. Phys. B Proc. Suppl.* **160** (2006) 131, ed. by J. Blumlein, S. Moch and T. Riemann, arXiv: [hep-ph/0607060](#) (cit. on p. 3).
- [50] E. Bothmann et al., *Event Generation with Sherpa 2.2*, *SciPost Phys.* **7** (2019) 034, arXiv: [1905.09127 \[hep-ph\]](#) (cit. on pp. 3, 4).
- [51] T. Gleisberg and S. Höche, *Comix, a new matrix element generator*, *JHEP* **12** (2008) 039, arXiv: [0808.3674 \[hep-ph\]](#) (cit. on p. 3).
- [52] S. Schumann and F. Krauss, *A Parton shower algorithm based on Catani-Seymour dipole factorisation*, *JHEP* **03** (2008) 038, arXiv: [0709.1027 \[hep-ph\]](#) (cit. on pp. 3, 4).
- [53] S. Höche, F. Krauss, M. Schönherr and F. Siegert, *A critical appraisal of NLO+PS matching methods*, *JHEP* **09** (2012) 049, arXiv: [1111.1220 \[hep-ph\]](#) (cit. on p. 3).
- [54] S. Höche, F. Krauss, M. Schönherr and F. Siegert, *QCD matrix elements + parton showers. The NLO case*, *JHEP* **04** (2013) 027, arXiv: [1207.5030 \[hep-ph\]](#) (cit. on p. 3).

- [55] S. Catani, F. Krauss, R. Kuhn and B. R. Webber, *QCD Matrix Elements + Parton Showers*, **JHEP** **11** (2001) 063, arXiv: [hep-ph/0109231](#) (cit. on p. 3).
- [56] S. Höche, F. Krauss, S. Schumann and F. Siegert, *QCD matrix elements and truncated showers*, **JHEP** **05** (2009) 053, arXiv: [0903.1219 \[hep-ph\]](#) (cit. on p. 3).
- [57] F. Cascioli, P. Maierhofer and S. Pozzorini, *Scattering Amplitudes with Open Loops*, **Phys. Rev. Lett.** **108** (2012) 111601, arXiv: [1111.5206 \[hep-ph\]](#) (cit. on p. 3).
- [58] A. Denner, S. Dittmaier and L. Hofer, *Collier: A fortran-based complex one-loop library in extended regularizations*, **Comput. Phys. Commun.** **212** (2017) 220, arXiv: [1604.06792 \[hep-ph\]](#) (cit. on p. 3).
- [59] C. Anastasiou, L. J. Dixon, K. Melnikov and F. Petriello, *High precision QCD at hadron colliders: Electroweak gauge boson rapidity distributions at NNLO*, **Phys. Rev. D** **69** (2004) 094008, arXiv: [hep-ph/0312266](#) (cit. on p. 4).
- [60] ATLAS Collaboration, *Studies on top-quark Monte Carlo modelling for Top2016*, ATL-PHYS-PUB-2016-020, 2016, URL: <https://cds.cern.ch/record/2216168> (cit. on p. 4).
- [61] M. C. et al, *Top-pair production at the LHC through NNLO QCD and NLO EW*, **JHEP** **186** (2017) (cit. on p. 4).
- [62] R. D. Ball et al., *Parton distributions with LHC data*, **Nucl. Phys. B** **867** (2013) 244, arXiv: [1207.1303 \[hep-ph\]](#) (cit. on p. 4).
- [63] S. Frixione, E. Laenen, P. Motylinski, B. R. Webber and C. D. White, *Single-top hadroproduction in association with a W boson*, **JHEP** **07** (2008) 029, arXiv: [0805.3067 \[hep-ph\]](#) (cit. on p. 4).
- [64] T. Sjöstrand, S. Mrenna and P. Skands, *A brief introduction to PYTHIA 8.1*, **Comput. Phys. Commun.** **178** (2008) 852, arXiv: [0710.3820 \[hep-ph\]](#) (cit. on p. 4).
- [65] ATLAS Collaboration, *The Pythia 8 A3 tune description of ATLAS minimum bias and inelastic measurements incorporating the Donnachie–Landshoff diffractive model*, ATL-PHYS-PUB-2016-017, 2016, URL: <https://cds.cern.ch/record/2206965> (cit. on p. 4).
- [66] ATLAS Collaboration, *Performance of electron and photon triggers in ATLAS during LHC Run 2*, **Eur. Phys. J. C** **80** (2020) 47, arXiv: [1909.00761 \[hep-ex\]](#) (cit. on pp. 4, 9).
- [67] ATLAS Collaboration, *Performance of the ATLAS muon triggers in Run 2*, (2020), arXiv: [2004.13447 \[hep-ex\]](#) (cit. on pp. 4, 9).
- [68] ATLAS Collaboration, *Electron reconstruction and identification in the ATLAS experiment using the 2015 and 2016 LHC proton–proton collision data at $\sqrt{s} = 13$ TeV*, **Eur. Phys. J. C** **79** (2019) 639, arXiv: [1902.04655 \[hep-ex\]](#) (cit. on p. 4).
- [69] ATLAS Collaboration, *Muon reconstruction performance of the ATLAS detector in proton–proton collision data at $\sqrt{s} = 13$ TeV*, **Eur. Phys. J. C** **76** (2016) 292, arXiv: [1603.05598 \[hep-ex\]](#) (cit. on pp. 4, 5, 9).
- [70] ATLAS Collaboration, *Electron and photon performance measurements with the ATLAS detector using the 2015–2017 LHC proton–proton collision data*, **JINST** **14** (2019) P12006, arXiv: [1908.00005 \[hep-ex\]](#) (cit. on pp. 4, 9).
- [71] M. Cacciari, G. P. Salam and G. Soyez, *The anti- k_t jet clustering algorithm*, **JHEP** **04** (2008) 063, arXiv: [0802.1189 \[hep-ph\]](#) (cit. on p. 5).
- [72] ATLAS Collaboration, *Jet reconstruction and performance using particle flow with the ATLAS Detector*, **Eur. Phys. J. C** **77** (2017) 466, arXiv: [1703.10485 \[hep-ex\]](#) (cit. on p. 5).

- [73] ATLAS Collaboration, *Jet energy scale measurements and their systematic uncertainties in proton–proton collisions at $\sqrt{s} = 13$ TeV with the ATLAS detector*, *Phys. Rev. D* **96** (2017) 072002, arXiv: [1703.09665 \[hep-ex\]](#) (cit. on pp. 5, 9).
- [74] ATLAS Collaboration, *Identification and rejection of pile-up jets at high pseudorapidity with the ATLAS detector*, *Eur. Phys. J. C* **77** (2017) 580, arXiv: [1705.02211 \[hep-ex\]](#) (cit. on p. 5), Erratum: *Eur. Phys. J. C* **77** (2017) 712.
- [75] ATLAS Collaboration, *Optimisation and performance studies of the ATLAS b-tagging algorithms for the 2017-18 LHC run*, ATL-PHYS-PUB-2017-013, 2017, URL: <https://cds.cern.ch/record/2273281> (cit. on p. 5).
- [76] ATLAS Collaboration, *ATLAS b-jet identification performance and efficiency measurement with $t\bar{t}$ events in pp collisions at $\sqrt{s} = 13$ TeV*, *Eur. Phys. J. C* **79** (2019) 970, arXiv: [1907.05120 \[hep-ex\]](#) (cit. on pp. 5, 9).
- [77] ATLAS Collaboration, *Performance of missing transverse momentum reconstruction with the ATLAS detector using proton–proton collisions at $\sqrt{s} = 13$ TeV*, *Eur. Phys. J. C* **78** (2018) 903, arXiv: [1802.08168 \[hep-ex\]](#) (cit. on pp. 5, 8).
- [78] T. Plehn, D. L. Rainwater and D. Zeppenfeld, *A method for identifying $H \rightarrow \tau\tau \rightarrow e^{+-}\mu^{+-} + \text{missing } p(T)$ at the CERN LHC*, *Phys.Rev.* **D61** (2000) 093005, arXiv: [hep-ph/9911385 \[hep-ph\]](#) (cit. on p. 5).
- [79] F. Chollet et al., *Keras*, <https://keras.io>, 2015 (cit. on p. 5).
- [80] *TensorFlow: Large-Scale Machine Learning on Heterogeneous Systems*, Software available from tensorflow.org, 2015, URL: <https://www.tensorflow.org/> (cit. on p. 5).
- [81] V. D. Barger, R. Phillips and D. Zeppenfeld, *Mini - jet veto: A Tool for the heavy Higgs search at the LHC*, *Phys. Lett. B* **346** (1995) 106, arXiv: [hep-ph/9412276](#) (cit. on p. 5).
- [82] ATLAS Collaboration, *Object-based missing transverse momentum significance in the ATLAS Detector*, ATLAS-CONF-2018-038, 2018, URL: <https://cds.cern.ch/record/2630948> (cit. on p. 6).
- [83] ATLAS Collaboration, *Luminosity determination in pp collisions at $\sqrt{s} = 13$ TeV using the ATLAS detector at the LHC*, ATLAS-CONF-2019-021, 2019, URL: <https://cds.cern.ch/record/2677054> (cit. on p. 9).

Appendix

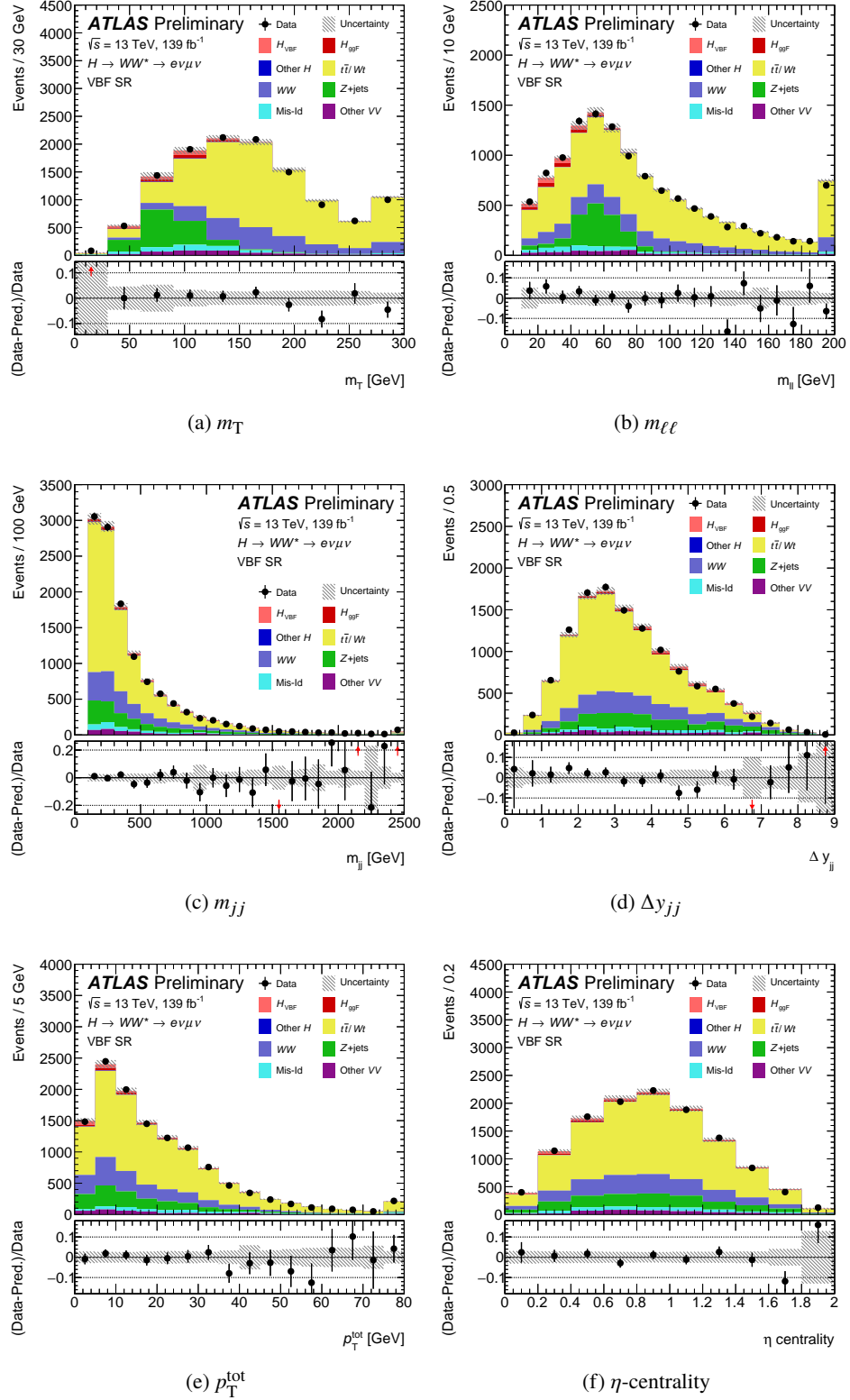


Figure 3: Post-fit distributions of m_T , $m_{\ell\ell}$, m_{jj} , Δy_{jj} , p_T^{tot} , and lepton η -centrality in the VBF signal region. The red arrows in the sub-panel denote where the central value of the data lies above or below the window. The yield for each process is normalized to its post-fit yield in the signal region. The hatched band shows the post-fit uncertainties derived from propagating the relative normalization uncertainty for each process to the post-fit distribution. Uncertainties due to shape variations are not accounted for in the uncertainty bands.

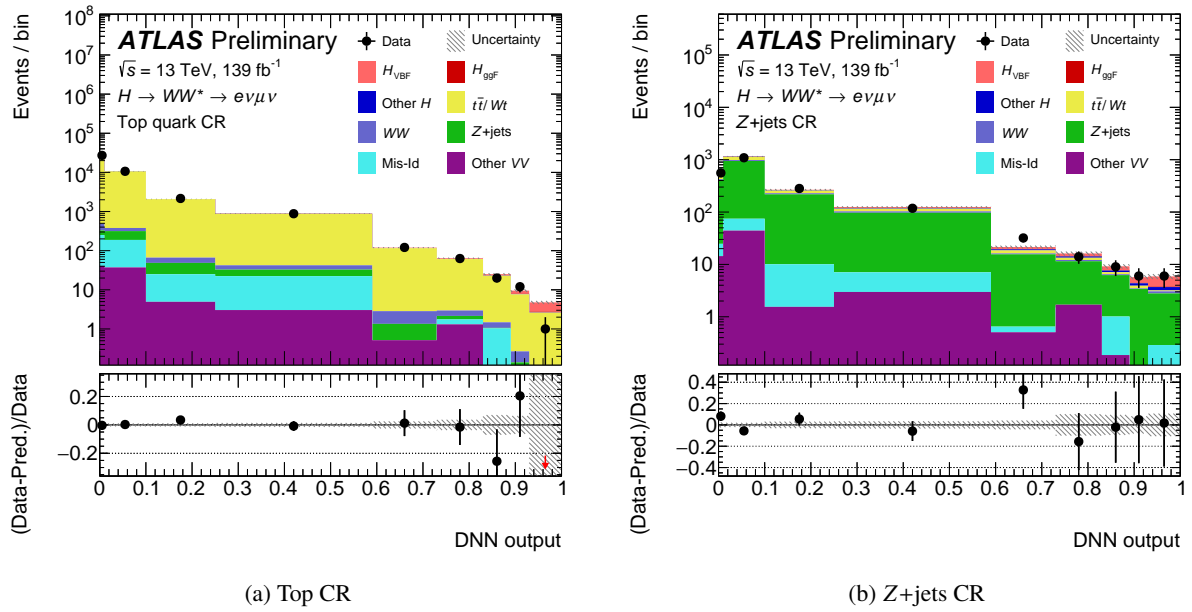
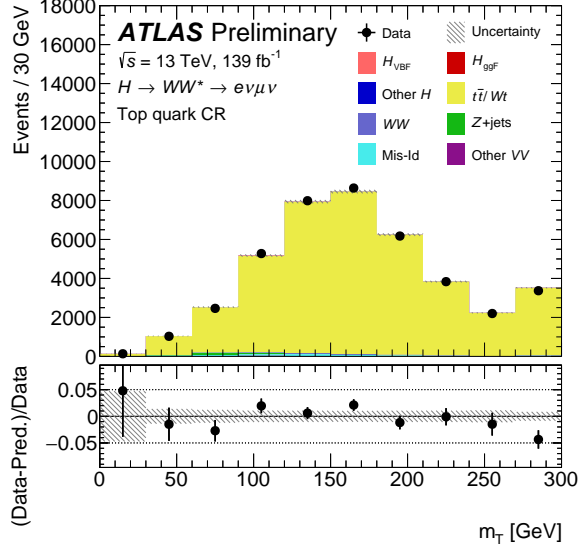
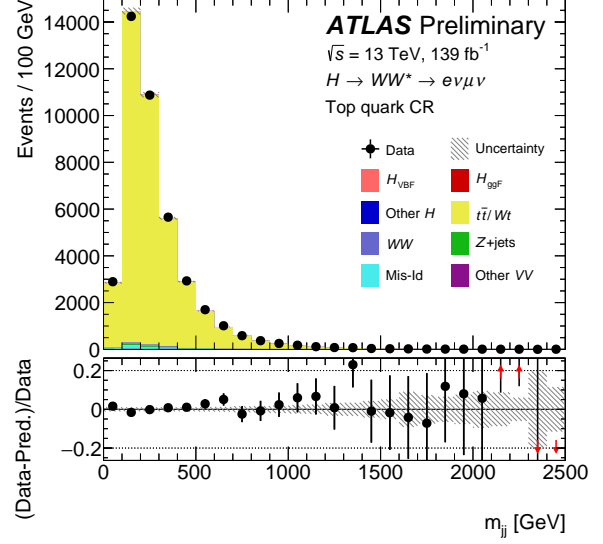


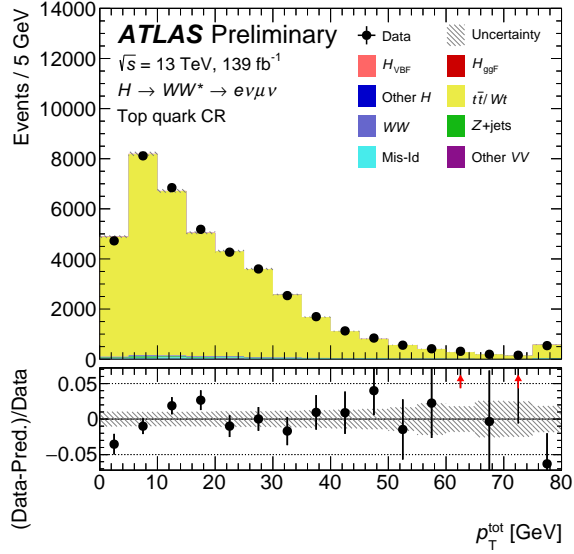
Figure 4: Post-fit distributions of the DNN output in the top quark CR and Z+jets CR. The red arrows in the sub-panel denote where the central value of the data lies above or below the window. The yield for each process is normalized to its post-fit yield in the relevant control region. The hatched band shows the post-fit uncertainties derived from propagating the relative normalization uncertainty for each process to the post-fit distribution. Uncertainties due to shape variations are not accounted for in the uncertainty bands. The bin boundaries correspond to the binning used in the statistical analysis except for the first 3 bins, which are all included in the first bin of the fit template but are separated here to illustrate the shape of the steeply-falling background.



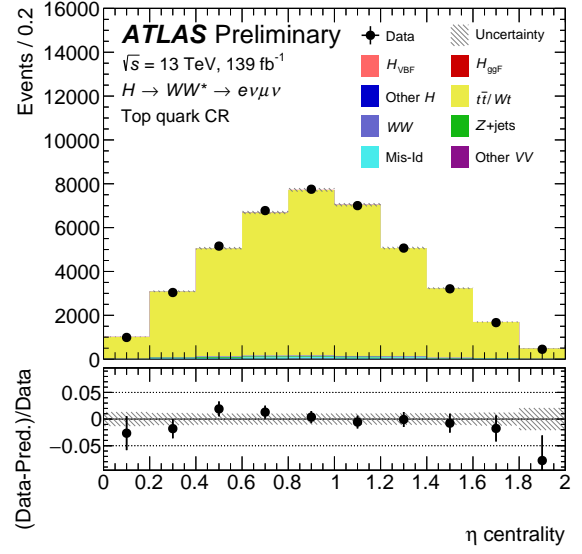
(a) m_T



(b) m_{jj}

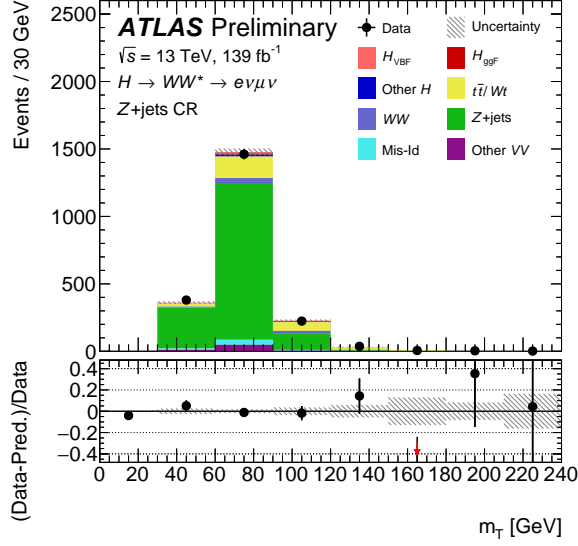


(c) p_T^{tot}

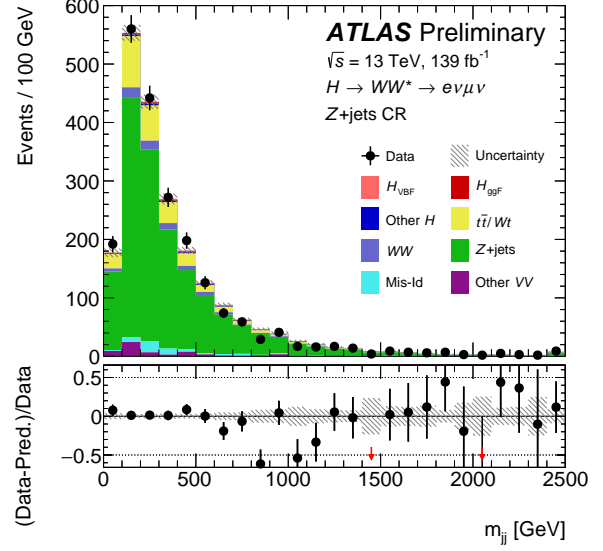


(d) η -centrality

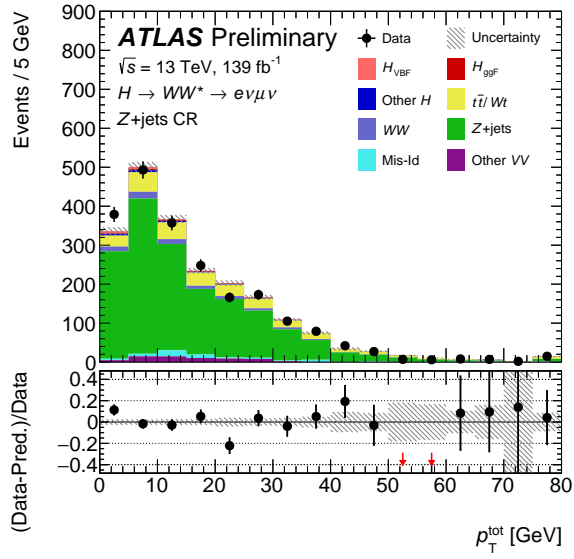
Figure 5: Post-fit distributions of m_T , m_{jj} , p_T^{tot} , and lepton η -centrality in the top quark CR. The red arrows in the sub-panel denote where the central value of the data lies above or below the window. The yield for each process is normalized to its post-fit yield in the top quark CR. The hatched band shows the post-fit uncertainties derived from propagating the relative normalization uncertainty for each process to the post-fit distribution. Uncertainties due to shape variations are not accounted for in the uncertainty bands.



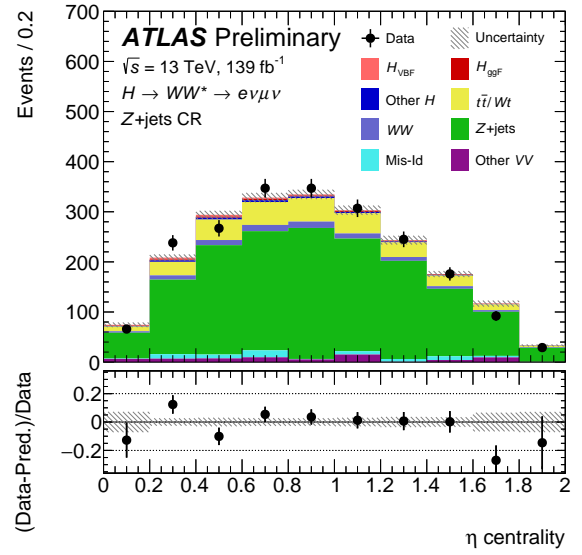
(a) m_T



(b) m_{jj}



(c) p_T^{tot}



(d) η -centrality

Figure 6: Post-fit distributions of m_T , m_{jj} , p_T^{tot} , and lepton η -centrality in the Z+jets CR. The yield for each process is normalized to its post-fit yield in the Z+jets CR. The hatched band shows the post-fit uncertainties derived from propagating the relative normalization uncertainty for each process to the post-fit distribution. Uncertainties due to shape variations are not accounted for in the uncertainty bands.

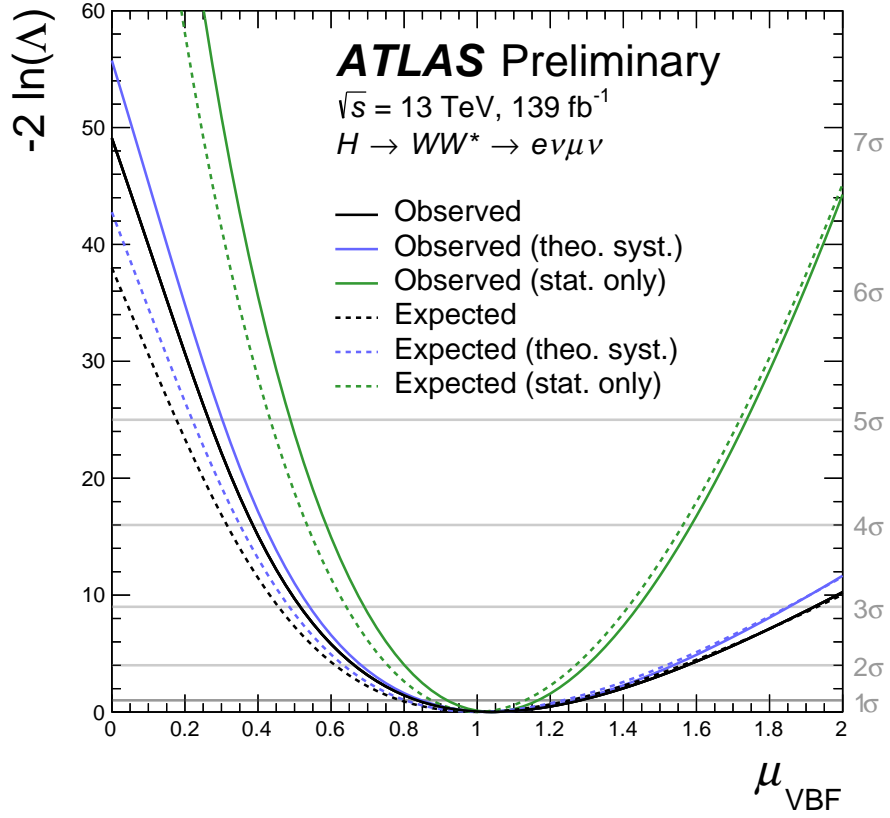


Figure 7: The observed (expected) negative log-likelihood as a function of the VBF signal strength, μ_{VBF} , with all systematics included (black lines), with all parameters fixed to their best-fit values except the ones corresponding to theoretical uncertainties (blue lines), with the same procedure applied to all systematic uncertainties, so that only statistical uncertainties remain (green lines). The gray horizontal lines and labels on the right show the levels of $-2\ln(\Lambda)$ that correspond to different confidence intervals for μ_{VBF} .

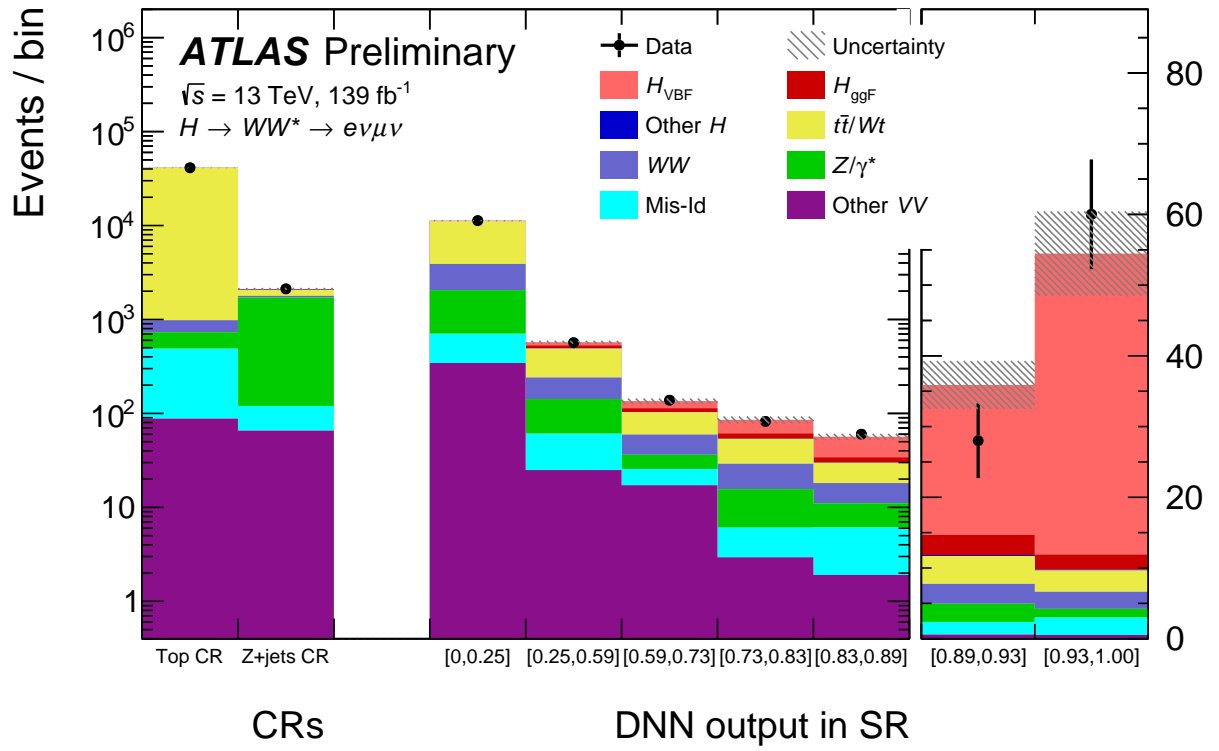


Figure 8: Post-fit distribution of the DNN output in the VBF signal region, together with the top and Z+jets control regions. The hatched band shows the total uncertainty of the signal and background modelled contributions.